BepiColombo Mio Observations of Low-Energy Ions During the First Mercury Flyby: Initial Results

Yuki Harada, Sae Aizawa, Yoshifumi Saito, Nicolas André, Moa Persson, Dominique Delcourt, L. Z. Hadid, Markus Fraenz, Shoichiro Yokota, Andréi Fedorov, et al.

BepiColombo Mio Observations of Low-Energy Ions During the First Mercury Flyby: Initial Results

Yuki Harada[1], Sae Aizawa[2], Yoshifumi Saito[3], Nicolas André[2], Moa Persson[2], Dominique Delcourt[4], Lina Z. Hadid[4], Markus Fraenz[5], Shoichiro Yokota[6], Andréi Fedorov[2], Wataru Miyake[7], Emmanuel Penou[2], Alain Barthe[2], Jean-André Sauvaud[2], Bruno Katra[4], Shoya Matsuda[8], Go Murakami[3]

[1]Department of Geophysics, Graduate School of Science, Kyoto University, Kyoto, Japan
[2]IRAP, CNRS-UPS-CNES, Toulouse, France
[3]Institute of Space and Astronautical Science, Japan Aerospace Exploration Agency, Japan
[4]Laboratoire de Physique des Plasmas (LPP), CNRS, Observatoire de Paris, Sorbonne Université, Université Paris Saclay, Ecole polytechnique, Institut Polytechnique de Paris, 91120 Palaiseau, France
[5]Max-Planck-Institute for Solar System Research, Göttingen, Germany
[6]Department of Earth and Space Science, Graduate School of Science, Osaka University, Japan
[7]Tokai University, 4-1-1 Kitakaname, Hiratsuka-shi, Kanagawa, Japan
[8]Graduate School of Natural Science and Technology, Kanazawa University, Kanazawa, Japan

Key Points:

- We present initial reports on low energy ion observations during BepiColombo's first Mercury flyby
- Mio observed large fluctuations of ion flux with time scales down to a few seconds around the magnetopause and within the magnetosphere
- Ion energy spectra obtained in the midnight magnetotail suggest the presence of an unexpectedly dense cold component

Corresponding author: Yuki Harada, `haraday@kugi.kyoto-u.ac.jp`

Abstract

We present initial results of low-energy ion observations from BepiColombo's first Mercury flyby. Unprecedentedly high time resolution measurements of low energy ions at Mercury by BepiColombo Mio reveal rapid (a few seconds) and large (1–2 orders of magnitude) fluctuations of ion flux around the magnetopause and within the magnetosphere. Around the magnetic equator in the pre-midnight magnetotail, Mio observed plasma sheet ions consistent with previous observations. In the midnight magnetotail near the closest approach, Mio observed the co-existence of high-energy (∼keV/q) and low-energy (<∼300 eV/q) ion components. The low-energy component is inferred to be cold with a temperature well below 100 eV and have a major contribution to the total density as opposed to previously reported cold tenuous ions. Future observations by Mio will provide insights into the sources, transport, and acceleration of the newly identified ion components.

Plain Language Summary

BepiColombo, launched on 20 October 2018, is now en route to Mercury. Along its 7-year journey to the Mercury orbit insertion, BepiColombo conducted, and will conduct, nine planetary flybys in total. This paper presents brand-new observations of ions (positively charged particles) in Mercury's magnetosphere by BepiColombo Mio during its first encounter with Mercury. Thanks to high-time resolution measurements by Mio, it is revealed that ions around Mercury change dramatically and rapidly just over a few seconds. Mio also observed an unexpectedly dense ion population with low energies, for which we do not have a definitive explanation yet. Future flyby and in-orbit observations by BepiColombo will provide key information for unraveling the dynamics and sources of ions in Mercury's magnetosphere.

1 Introduction

Driven by the intense solar wind in the inner heliosphere, Mercury's magnetosphere is known to be small and dynamic. Mercury's weak dipole magnetic field of 190 nT-R_M^3 (Anderson et al., 2012), where R_M is Mercury's radius, and high solar wind dynamic pressures at Mercury's orbit (∼5–10 times higher at 0.31–0.47 AU than those at 1 AU) result in small spatial dimensions of the magnetosphere with an average subsolar standoff distance of 1.45 R_M (Winslow et al., 2013). Consequently, time scales of magnetospheric dynamics driven by the solar wind are considerably short at Mercury (e.g., Siscoe et al., 1975). Our understanding of Mercury's magnetosphere has been greatly advanced thanks to the two previous missions to Mercury, Mariner 10 and MESSENGER, but there remain many open questions as to the plasma sources, energy and mass transport, and particle acceleration processes in Mercury's magnetosphere, and their coupling to the exosphere, surface, and interior of the planet (J. Slavin, 2004; Raines et al., 2015; W. Sun, Dewey, et al., 2022).

BepiColombo conducted its first Mercury flyby on 1 October 2021. Near the closest approach, BepiColombo traversed low-altitude regions in the southern hemisphere, which were poorly sampled, or even never visited, by Mariner 10 and MESSENGER. During the flyby, the two spacecraft of BepiColombo, Mio and Mercury Planetary Orbiter, were in a stacked configuration (Murakami et al., 2020), and the Mercury Plasma Particle Experiment (MPPE) onboard Mio successfully measured low-energy ions and electrons in the vicinity of Mercury. This paper reports on initial results from low-energy ion observations by Mio during the first Mercury flyby. A broader overview of simultaneous observations of low-energy ions and electrons in Mercury's magnetosphere by Mio will be reported elsewhere.

2 Data and Model

We analyze low-energy ion data obtained by the Mercury Ion Analyzer (MIA), one of the seven sensors of the MPPE consortium onboard Mio (Saito et al., 2021). An energy-time (Et) spectrogram with a nominal time resolution of 4 s (which is the planned spin period) is generated from the MIA "Et" data product. This data product contains ion energy spectra for four directions according to spin phase such that energy spectra will be obtained separately for ions traveling approximately sunward, anti-sunward, dawnward, and duskward in the nominal in-orbit operation (see Figure 31 and Table 12 of Saito et al. (2021)). In a given spin, a full spin period is divided into 8 groups of spin sectors, spin sector groups 0–7. MIA generates the Et product for 4 directions consisting of spin sector groups 0 and 7 (direction 1), 1 and 2 (direction 2), 3 and 4 (direction 3), and 5 and 6 (direction 4). During the cruise phase, we can exploit this functionality to effectively enhance the time resolution from 4 s down to 1 s because the spacecraft does not spin and the field of view does not change rapidly during the cruise and flyby observations. By ordering the three sequential data points, namely directions 2 through 4, according to the data acquisition times and discarding the direction 1, which accumulates non-sequential data points from the first 1/8 and last 1/8 of the spin period, we obtain "quasi-1 s" resolution data recorded at a cadence of 1 s, 1 s, 2 s, 1 s, 1 s, 2 s, and so on. Due to the ongoing calibration of the lowest energies of the MIA energy sweep, we restrict our analysis to the MIA data above 80 eV/q in this paper. We note that mass-resolved ion data from the Mass Spectrum Analyzer (MSA) are unavailable near the first closest approach to Mercury. As Mio is behind the thermal shield during the cruise phase, most of the field of view (FOV) of MIA is blocked (Murakami et al., 2020), and we need to consider its unblocked, effective FOV when interpreting the data.

To aid the interpretation of the particle data, we utilize an empirical magnetospheric magnetic field model (KT17) developed by Korth et al. (2017). The KT17 model is parameterized by the heliocentric distance of Mercury and the disturbance index (DI) of Mercury's magnetosphere (Anderson et al., 2013). For the former, we use the instantaneous heliocentric distance at the time of the observation. For the latter, we chose DI of 100, which represents the most compressed state of the magnetosphere that can be expressed by the model, based on locations of outbound magnetopause crossings identified from the ion observations as described in the following section. We conducted tests with different choices of DI, which did not qualitatively change the results presented in this paper.

Unless otherwise noted, we use the aberrated Mercury Solar Magnetospheric (MSM) coordinate system, which takes into account the northward offset of Mercury's dipole and the solar wind aberration according to the instantaneous orbital velocity of Mercury and a typical solar wind speed of 400 km/s in the same manner as Korth et al. (2015).

3 Observations

Figure 1 shows the observation geometry of Mio's first Mercury flyby on 1 October 2021. As seen in Figures 1a, 1c, and 1d, the spacecraft entered the duskside magnetotail from the flank magnetosheath around 23:10 UTC, crossed the magnetic equator ($Z_{MSM} = 0$) in the pre-midnight magnetotail at 23:17:37 UTC, traveled from midnight to dawn in the southern MSM hemisphere around 23:30–23:40 UTC near the closest approach, and exited from the post-dawn magnetosphere into the dayside magnetosheath around 23:41 UTC. Magnetic field line mapping with the KT17 model suggests that the spacecraft was located on closed field lines connected to the magnetic equator at radial distances of $\sim$1.7–4.9R_M (Figure 1a) and to the surface foot points near the open-closed boundary (Figure 1b).

Figure 2 presents the overall time series of MIA data along with predictions from the KT17 model. The white areas in Figure 2a represent data gaps. The colored labels on top of Figure 2a indicate plasma regions inferred from the ion data and the observation geometry. For selected time intervals (indicated by the horizontal bars with labels of "3a"−"3h" in Figures 2a and 2b), we present detailed characteristics of the ion data in Figure 3. In the following, we investigate ion signatures in each region.

Mio was presumably located in the magnetosheath before 23:07:45 UTC. During this time interval, MIA observed a relatively low flux of ions at a few 100 eV/q (Figure 2a). This signature can be interpreted as a small portion of magnetosheath ions detected by MIA's limited FOV, which was directed mostly duskward (Figure 1a).

We infer that Mio crossed a transition region from the magnetosheath into the magnetosphere during 23:07:45–23:14:06 UTC. During 23:07:45–23:09:41 UTC, MIA measured intermittent flux enhancements at broad energies up to several keV/q superimposed on the continuous presence of a few 100 eV ions (Figure 2a). Figure 3e shows a zoom-in of the intermittent flux enhancements. The durations of the individual flux enhancements range from several seconds to a few tens of seconds, with the spacing of similar durations. Subsequently, MIA observed sustained broad energy spectra up to several keV/q along with a relatively high flux of low-energy ions at $<\sim$ 300 eV/q during 23:13:04–23:14:06 UTC (Figure 2a). Figure 3a shows a representative energy spectrum at this time along with a two-component (a cold Maxwellian and a hot kappa distribution (Vasyliunas, 1968)) fitting result. When fitting the data, we assume that ions are isotropic and are all protons. We note that if planetary heavy ions are present, their fractional density is underestimated by a factor of $\sqrt{m/q}$ under the proton-only assumption (McFadden et al., 2008). In Figure 3a, it is seen that the observed spectrum is well represented by a superposition of a relatively cold, dense component and a hot, tenuous component. The hot component with broad energies is likely to be magnetospheric ions. The intermittent appearance of the hot ions (Figure 3e) and the mixture of relatively cold and hot ions (Figure 3a) suggest a structured and gradual transition from the flank magnetosheath into the low-latitude magnetotail encountered by Mio rather than a single crossing of a sharp boundary.

Mio crossed the magnetic equator in the pre-midnight magnetotail (Figure 1) at 23:17:37 UTC (indicated by the vertical black line in Figure 2). Around this time, MIA observed broad energy spectra, presumably of plasma sheet ions (Figure 2a). Figure 3b shows an energy spectrum obtained just before the magnetic equator crossing. We observe a one-component distribution well represented by a kappa distribution.

Next, we investigate ion signatures observed at low altitudes below 1000 km near the closest approach. Around 23:30 UTC, we observe the co-existence of two well-separated components, one at $\sim$1–3 keV/q and the other at $<\sim$300 eV/q (labeled "3c" in Figure 2a) on field lines connected to the midnight magnetotail (Figure 1). Figure 3c shows the energy spectrum of the two-component ions. We observe two humps in the energy spectrum, which clearly deviates from a single Maxwellian or kappa distribution. The colored lines show two-Maxwellian fits to the data (for this spectrum, the hot component has too few data points to be adequately fitted by a kappa distribution). The cold component is inferred to have a low temperature (well below 100 eV) and relatively high density compared to the hot component. After the hot component disappeared at 23:30:20 UTC, a similar two-component signature reemerged around 23:32 UTC, and subsequently, the hot and cold components merged into one component at broad energies of $\sim$100–3000 eV/q (labeled "3d" in Figure 2a). As shown in Figure 3d, the merged component is characterized by a single Maxwellian-like distribution with a large kappa value.

The MIA quasi-1 s data reveal that the $\sim$keV/q ion component comprises finer substructures. Figures 3f and 3g show zoom-ins of flux variations at representative energies (during the time intervals labeled "3f" and "3g" in Figure 2b). In the quasi-1 s data, we observe large, rapid flux fluctuations with ∼1–2 orders of magnitude variations within just a few seconds. This time scale of the rapid flux variations corresponds to several proton gyroperiods and to a fraction of the gyroradius divided by the spacecraft velocity (see the horizontal bars in Figures 3f and 3g). Thus, if these substructures originate entirely from temporal variations, they represent proton-scale time variations. If the observed variations are purely spatial and result from crossings of static structures, they represent sub-proton-scale spatial structures (see Figure 2e for ion gyroradii in kilometers).

We also observe signatures suggestive of absorption of magnetospheric ions by the surface of Mercury. Between the two vertical dashed lines in Figures 2a and 2b, the observed ion flux is reduced by a factor of >10 compared to that at the adjacent times. The reduced ion flux coincides with the time interval during which the effective FOV of MIA is predicted to be within the loss cone according to the KT17 model (Figure 2c). The predicted size of the loss cone is relatively large because of the strong local magnetic fields at low altitudes (Figures 2d and 2e).

We next examine the outbound magnetopause crossing. Overall, the peak energy shifted from ∼1 keV/q down to ∼200 eV/q during 23:40:30–23:41:10 UTC (Figure 2a). The ∼1 keV/q peak energy is consistent with the ion population observed well within the magnetosphere. The relatively low energy peak at ∼200 eV/q and intense ion flux exceeding 10^8 eV/cm^2/s/sr/eV observed after 23:41:00 UTC suggest that the spacecraft crossed the magnetopause into the magnetosheath. Note that the direction of MIA's FOV is more favorable for detection of the bulk component of magnetosheath ion flows deflected along the magnetopause in the outbound magnetosheath as opposed to the inbound magnetosheath (Figure 1). Figure 3h presents the time variation of 210 eV/q ion flux around the inferred magnetopause crossing. The MIA data clearly resolve multiple crossings, exhibiting at least 3 crossings within a 40 s interval.

4 Discussion

We now discuss Mio's observations of low-energy ions in comparison with relevant observations at Mercury by the two previous missions, Mariner 10 and MESSENGER, and provide implications for future observations by BepiColombo.

Around the magnetic equator in the pre-midnight magnetotail, MIA observed a broad energy spectrum characterized by a kappa distribution with a density of ∼16 cm^{-3}, temperature of ∼470 eV, and kappa of ∼4.8 (Figure 3b). These parameters are generally in accordance with previously reported results (Gershman et al., 2014; Zhao et al., 2020). Specifically, the density (temperature) is near the higher (lower) end of the MESSENGER observations in the pre-midnight plasma sheet reported by Gershman et al. (2014). They also reported that the high-density, low-temperature plasma sheet tends to be observed under slower (and generally denser) solar wind conditions. According to Figure 1 of Gershman et al. (2014), the MIA observation of relatively cold (∼470 eV ∼ 5.5 MK), dense (∼16 cm^{-3}) plasma sheet may indirectly imply a slow (<∼300 km/s) and generally dense condition of the upstream solar wind during the flyby.

MIA measured the two components of high-energy (∼1 keV/q) and low-energy (<∼300 eV/q) ions (Figure 3c) around midnight in the magnetotail. The cold component provides a predominant contribution to the total density (Figure 3c) as opposed to the reportedly small cold to total density ratios (∼10%) based on case studies (W. J. Sun et al., 2017) and average proton energy spectra in various spatial regions sampled by MESSENGER (Zhao et al., 2020). The two-component energy spectra observed by MIA are reminiscent of multiple ion beams observed in the terrestrial Plasma Sheet Boundary Layer (PSBL) (Eastman et al., 1984, 1985; Nakamura et al., 1992; Hirahara et al., 1994; Parks et al., 2001). In the terrestrial PSBL, the high-energy component often represents a high-speed ion flow, while the low-energy component comprises cold ions of ionospheric origin. In this regard, a notable difference between Mercury and Earth is the lack of a significant ionospheric source at Mercury. The sources of magnetospheric plasma at Mercury are thought to be mainly provided by the entry of the solar wind plasma (Sundberg et al., 2012; Korth et al., 2014; DiBraccio, Slavin, Raines, et al., 2015; Jasinski et al., 2017) with a minor number density contribution from planetary heavy ions on average (Gershman et al., 2014). Thus, the cold dense component could be either a low-energy portion of magnetosheath ions that are transported to the low-altitude midnight magnetotail or planetary heavy ions that are denser than previously thought. To elucidate the sources and transport processes of the two-component ions, 3D velocity distribution functions and ion composition should be investigated in detail, much as done for the terrestrial magnetotail. It is also remarkable that the hot component ions exhibit large variability over several proton gyroperiods in time and within a fraction of the proton gyroradius in space, implying their fundamentally kinetic nature. There appear to be plenty of possible drivers of the rapid ion flux variations in Mercury's magnetosphere, which contains a variety of rapid ($<\sim$10 s) fluctuations such as flux transfer events (FTEs) (e.g., J. A. Slavin et al., 2012), magnetotail flux ropes (e.g., DiBraccio, Slavin, Imber, et al., 2015), cross-tail current sheet flapping (Poh et al., 2020; Zhang et al., 2020), and Pi2-like pulsations (W.-J. Sun et al., 2015). The properties of the relatively dense, cold ions and the highly variable, hot ions in Mercury's magnetosphere should be systematically investigated with future observations.

Neither of the inbound and outbound magnetopause crossings was a simple, single crossing of a sharp boundary. The high-time-resolution ion measurements by MIA indicate complex and rapid variations of ions of magnetosheath and magnetospheric origins. Rapid, multiple magnetopause crossings at Mercury have been identified and analyzed mainly by high-time resolution magnetic field measurements, and were interpreted as quick relative motion of the magnetopause (Ness et al., 1974; DiBraccio et al., 2013; J. A. Slavin et al., 2014) and as a spatially structured and temporally evolving boundary such as Kelvin-Helmholtz waves and FTEs at the magnetopause (J. A. Slavin et al., 2008, 2012; Sundberg et al., 2012; Liljeblad et al., 2014; Gershman et al., 2015; Aizawa et al., 2020). Combination of high-time-resolution ion and magnetic field measurements by BepiColombo will shed new light on the dynamics of the magnetospheric boundaries at Mercury.

During the time interval in which the MIA FOV is directed within the loss cone predicted by the KT17 model, the ion flux measured by MIA is $>$10 times lower than that at the adjacent times. This is in agreement with the ion loss cone observed by MESSENGER within Mercury's magnetosphere (Winslow et al., 2014; Zhao et al., 2020, 2022), though we cannot conclusively confirm the ion loss cone from the flyby MIA data due to the limited FOV. In-orbit observations by MIA will provide the full 4π coverage, and in combination with magnetic field measurements, comprehensive energy–pitch-angle distributions of ions will be available. Such data will enable ion reflectometry to remotely probe the surface magnetic field strength (Winslow et al., 2014) and possibly electrostatic potentials (Harada et al., 2017), as well as investigate surface-emitted ions such as backscattered and sputtered ions (Saito et al., 2008; Yokota et al., 2009; Raines et al., 2014; W. Sun, Slavin, et al., 2022).

5 Conclusions

This paper presents initial reports on low-energy ion measurements by Mio during the first Mercury flyby. The high-time resolution data obtained by MIA highlight the dynamic nature of low-energy ions in Mercury's magnetosphere. Both of the inbound and outbound magnetopause crossings show the complex behavior of magnetosheath and magnetospheric ions as opposed to a simple, sharp boundary singly crossed by the spacecraft. Around the magnetic equator in the pre-midnight magnetotail, MIA observed plasma sheet ions with broad energies. The inferred density (temperature) of the pre-midnight plasma sheet ions is near the higher (lower) end of the reported range of the MESSENGER results, possibly resulting from a generally slow and dense condition of the upstream solar wind. In the midnight magnetosphere, MIA observed the co-existence of high-energy ($\sim$ keV/q) and low-energy ($<\sim$300 eV/q) components. The low-energy component is inferred to be cold ($T < 100$ eV) and have a major contribution to the total density in contrast to the previous results suggesting only a minor density contribution by cold ions. The hot ion flux shows ∼1–2 orders of magnitude variations just over a few seconds, suggesting the presence of proton-scale time variations and/or sub-proton-scale spatial structures. The sources, transport mechanisms, and acceleration processes of the two-component ions remain elusive. As demonstrated by the rich information derived from Mio's particle measurements with the still limited capabilities during the first flyby, future flyby and in-orbit observations by BepiColombo will provide revolutionary data for understanding the structure and dynamics of Mercury's magnetosphere.

6 Open Research

The MIA data used in this paper are archived and publicly available (Harada et al., 2022).

Acknowledgments

French co-authors acknowledge the support of CNES for the BepiColombo mission. MP is funded by the European Union's Horizon 2020 programme under grant agreement No 871149 for Europlanet 2024 RI.

References

Aizawa, S., Raines, J. M., Delcourt, D., Terada, N., & André, N. (2020). Messenger observations of planetary ion characteristics in the vicinity of kelvin-helmholtz vortices at mercury. *Journal of Geophysical Research: Space Physics*, *125*(10), e2020JA027871. Retrieved from https://agupubs.onlinelibrary.wiley.com/doi/abs/10.1029/2020JA027871 (e2020JA027871 2020JA027871) doi: https://doi.org/10.1029/2020JA027871

Anderson, B. J., Johnson, C. L., & Korth, H. (2013). A magnetic disturbance index for Mercury's magnetic field derived from MESSENGER Magnetometer data. *Geochem. Geophys. Geosyst.*, *14*(9), 3875–3886. Retrieved from http://dx.doi.org/10.1002/ggge.20242 doi: 10.1002/ggge.20242

Anderson, B. J., Johnson, C. L., Korth, H., Winslow, R. M., Borovsky, J. E., Purucker, M. E., ... McNutt, R. L. (2012). Low-degree structure in Mercury's planetary magnetic field. *J. Geophys. Res.*, *117*, E00L12. doi: 10.1029/2012JE004159

DiBraccio, G. A., Slavin, J. A., Boardsen, S. A., Anderson, B. J., Korth, H., Zurbuchen, T. H., ... Solomon, S. C. (2013). MESSENGER observations of magnetopause structure and dynamics at Mercury. *J. Geophys. Res.*, *118*(3), 997–1008. Retrieved from http://dx.doi.org/10.1002/jgra.50123 doi: 10.1002/jgra.50123

DiBraccio, G. A., Slavin, J. A., Imber, S. M., Gershman, D. J., Raines, J. M., Jackman, C. M., ... Solomon, S. C. (2015). *Planet. Space Sci.*, *115*, 77 - 89. Retrieved from http://www.sciencedirect.com/science/article/pii/S0032063314004085 doi: 10.1016/j.pss.2014.12.016

DiBraccio, G. A., Slavin, J. A., Raines, J. M., Gershman, D. J., Tracy, P. J., Boardsen, S. A., ... Solomon, S. C. (2015). First observations of Mercury's plasma mantle by MESSENGER. *Geophys. Res. Lett.*, *42*(22), 9666–

9675. Retrieved from http://dx.doi.org/10.1002/2015GL065805 doi: 10.1002/2015GL065805

Eastman, T. E., Frank, L. A., & Huang, C. Y. (1985). The boundary layers as the primary transport regions of the earth's magnetotail. *Journal of Geophysical Research: Space Physics*, *90*(A10), 9541-9560. Retrieved from https://agupubs.onlinelibrary.wiley.com/doi/abs/10.1029/JA090iA10p09541 doi: https://doi.org/10.1029/JA090iA10p09541

Eastman, T. E., Frank, L. A., Peterson, W. K., & Lennartsson, W. (1984). The plasma sheet boundary layer. *Journal of Geophysical Research: Space Physics*, *89*(A3), 1553-1572. Retrieved from https://agupubs.onlinelibrary.wiley.com/doi/abs/10.1029/JA089iA03p01553 doi: https://doi.org/10.1029/JA089iA03p01553

Gershman, D. J., Raines, J. M., Slavin, J. A., Zurbuchen, T. H., Sundberg, T., Boardsen, S. A., … Solomon, S. C. (2015). Messenger observations of multiscale kelvin-helmholtz vortices at mercury. *Journal of Geophysical Research: Space Physics*, *120*(6), 4354-4368. Retrieved from https://agupubs.onlinelibrary.wiley.com/doi/abs/10.1002/2014JA020903 doi: https://doi.org/10.1002/2014JA020903

Gershman, D. J., Slavin, J. A., Raines, J. M., Zurbuchen, T. H., Anderson, B. J., Korth, H., … Solomon, S. C. (2014). Ion kinetic properties in mercury's pre-midnight plasma sheet. *Geophysical Research Letters*, *41*(16), 5740-5747. Retrieved from https://agupubs.onlinelibrary.wiley.com/doi/abs/10.1002/2014GL060468 doi: https://doi.org/10.1002/2014GL060468

Harada, Y., Aizawa, S., Saito, Y., André, N., Persson, M., Delcourt, D., … Murakami, G. (2022, July). *BepiColombo Mio MIA Data During the First Mercury Flyby.* Zenodo. Retrieved from https://doi.org/10.5281/zenodo.6797894 doi: 10.5281/zenodo.6797894

Harada, Y., Poppe, A. R., Halekas, J. S., Chamberlin, P. C., & McFadden, J. P. (2017). Photoemission and electrostatic potentials on the dayside lunar surface in the terrestrial magnetotail lobes. *Geophys. Res. Lett.*, *44*(11), 5276–5282. Retrieved from http://dx.doi.org/10.1002/2017GL073419 doi: 10.1002/2017GL073419

Hirahara, M., Nakamura, M., Terasawa, T., Mukai, T., Saito, Y., Yamamoto, T., … Kokubun, S. (1994). Acceleration and heating of cold ion beams in the plasma sheet boundary layer observed with geotail. *Geophysical Research Letters*, *21*(25), 3003-3006. Retrieved from https://agupubs.onlinelibrary.wiley.com/doi/abs/10.1029/94GL02109 doi: https://doi.org/10.1029/94GL02109

Jasinski, J. M., Slavin, J. A., Raines, J. M., & DiBraccio, G. A. (2017). Mercury's solar wind interaction as characterized by magnetospheric plasma mantle observations with messenger. *Journal of Geophysical Research: Space Physics*, *122*(12), 12,153-12,169. Retrieved from https://agupubs.onlinelibrary.wiley.com/doi/abs/10.1002/2017JA024594 doi: https://doi.org/10.1002/2017JA024594

Korth, H., Anderson, B. J., Gershman, D. J., Raines, J. M., Slavin, J. A., Zurbuchen, T. H., … McNutt Jr., R. L. (2014). Plasma distribution in mercury's magnetosphere derived from messenger magnetometer and fast imaging plasma spectrometer observations. *Journal of Geophysical Research: Space Physics*, *119*(4), 2917-2932. Retrieved from https://agupubs.onlinelibrary.wiley.com/doi/abs/10.1002/2013JA019567 doi: https://doi.org/10.1002/2013JA019567

Korth, H., Johnson, C. L., Philpott, L., Tsyganenko, N. A., & Anderson, B. J. (2017). A Dynamic Model of Mercury's Magnetospheric Magnetic Field. *Geophys. Res. Lett.*, *44*(20), 10,147-10,154. Retrieved from https://agupubs.onlinelibrary.wiley.com/doi/abs/10.1002/2017GL074699 doi:

10.1002/2017GL074699

Korth, H., Tsyganenko, N. A., Johnson, C. L., Philpott, L. C., Anderson, B. J., Al Asad, M. M., … McNutt, R. L. (2015). Modular model for Mercury's magnetospheric magnetic field confined within the average observed magnetopause. *J. Geophys. Res.*, *120*(6), 4503-4518. Retrieved from https://agupubs.onlinelibrary.wiley.com/doi/abs/10.1002/2015JA021022 doi: 10.1002/2015JA021022

Liljeblad, E., Sundberg, T., Karlsson, T., & Kullen, A. (2014). Statistical investigation of Kelvin-Helmholtz waves at the magnetopause of Mercury. *J. Geophys. Res.*, *119*(12), 9670-9683. Retrieved from https://agupubs.onlinelibrary.wiley.com/doi/abs/10.1002/2014JA020614 doi: 10.1002/2014JA020614

McFadden, J. P., Carlson, C. W., Larson, D., Bonnell, J., Mozer, F., Angelopoulos, V., … Auster, U. (2008, DEC). THEMIS ESA First Science Results and Performance Issues [Review]. *Space Sci. Rev.*, *141*(1-4), 477-508. doi: {10.1007/s11214-008-9433-1}

Murakami, G., Hayakawa, H., Ogawa, H., Matsuda, S., Seki, T., Kasaba, Y., … Fujimoto, M. (2020). Mio—first comprehensive exploration of mercury's space environment: Mission overview. *Space Science Reviews*, *216*(7), 113. Retrieved from https://doi.org/10.1007/s11214-020-00733-3 doi: 10.1007/s11214-020-00733-3

Nakamura, M., Paschmann, G., Baumjohann, W., & Sckopke, N. (1992). Ion distributions and flows in and near the plasma sheet boundary layer. *Journal of Geophysical Research: Space Physics*, *97*(A2), 1449-1460. Retrieved from https://agupubs.onlinelibrary.wiley.com/doi/abs/10.1029/91JA02361 doi: https://doi.org/10.1029/91JA02361

Ness, N. F., Behannon, K. W., Lepping, R. P., Whang, Y. C., & Schatten, K. H. (1974). Magnetic Field Observations near Mercury: Preliminary Results from Mariner 10. *Science*, *185*(4146), 151-160. Retrieved from http://www.sciencemag.org/content/185/4146/151.abstract doi: 10.1126/science.185.4146.151

Parks, G. K., Chen, L. J., Fillingim, M., & McCarthy, M. (2001). Kinetic characterization of plasma sheet dynamics. *Space Science Reviews*, *95*(1), 237–255. Retrieved from https://doi.org/10.1023/A:1005206701965 doi: 10.1023/A:1005206701965

Poh, G., Sun, W., Clink, K. M., Slavin, J. A., Dewey, R. M., Jia, X., … Espley, J. R. (2020). Large-amplitude oscillatory motion of mercury's cross-tail current sheet. *Journal of Geophysical Research: Space Physics*, *125*(7), e2020JA027783. Retrieved from https://agupubs.onlinelibrary.wiley.com/doi/abs/10.1029/2020JA027783 (e2020JA027783 2020JA027783) doi: https://doi.org/10.1029/2020JA027783

Raines, J. M., DiBraccio, G. A., Cassidy, T. A., Delcourt, D. C., Fujimoto, M., Jia, X., … Wurz, P. (2015). Plasma sources in planetary magnetospheres: Mercury. *Space Science Reviews*, *192*(1), 91–144. Retrieved from https://doi.org/10.1007/s11214-015-0193-4 doi: 10.1007/s11214-015-0193-4

Raines, J. M., Gershman, D. J., Slavin, J. A., Zurbuchen, T. H., Korth, H., Anderson, B. J., & Solomon, S. C. (2014). Structure and dynamics of Mercury's magnetospheric cusp: MESSENGER measurements of protons and planetary ions. *J. Geophys. Res.*, *119*(8), 6587-6602. Retrieved from https://agupubs.onlinelibrary.wiley.com/doi/abs/10.1002/2014JA020120 doi: 10.1002/2014JA020120

Saito, Y., Delcourt, D., Hirahara, M., Barabash, S., André, N., Takashima, T., … Team, B. M. (2021). Pre-flight calibration and near-earth commissioning results of the mercury plasma particle experiment (mppe) onboard mmo (mio). *Space Science Reviews*, *217*(5), 70. Retrieved from https://doi.org/10.1007/s11214-021-00839-2 doi: 10.1007/s11214-021-00839-2

Saito, Y., Yokota, S., Tanaka, T., Asamura, K., Nishino, M. N., Fujimoto, M., . . . Terasawa, T. (2008). Solar Wind Proton Reflection at the Lunar Surface: Low Energy Ion Measurement by MAP-PACE Onboard SELENE (KAGUYA). *Geophys. Res. Lett.*, *35*, L24205. doi: 10.1029/2008GL036077

Siscoe, G. L., Ness, N. F., & Yeates, C. M. (1975). Substorms on Mercury? *J. Geophys. Res.*, *80*(31), 4359-4363. Retrieved from https://agupubs.onlinelibrary.wiley.com/doi/abs/10.1029/JA080i031p04359 doi: 10.1029/JA080i031p04359

Slavin, J. (2004). Mercury's magnetosphere . *Adv. Space Res.*, *33*(11), 1859 - 1874. Retrieved from http://www.sciencedirect.com/science/article/pii/S0273117704000092 doi: 10.1016/j.asr.2003.02.019

Slavin, J. A., Acuña, M. H., Anderson, B. J., Baker, D. N., Benna, M., Gloeckler, G., . . . Zurbuchen, T. H. (2008). Mercury's Magnetosphere After MESSENGER's First Flyby. *Science*, *321*(5885), 85-89. Retrieved from http://www.sciencemag.org/content/321/5885/85.abstract doi: 10.1126/science.1159040

Slavin, J. A., DiBraccio, G. A., Gershman, D. J., Imber, S. M., Poh, G. K., Raines, J. M., . . . Solomon, S. C. (2014). MESSENGER observations of Mercury's dayside magnetosphere under extreme solar wind conditions. *J. Geophys. Res.*, *119*(10), 8087-8116. Retrieved from https://agupubs.onlinelibrary.wiley.com/doi/abs/10.1002/2014JA020319 doi: 10.1002/2014JA020319

Slavin, J. A., Imber, S. M., Boardsen, S. A., DiBraccio, G. A., Sundberg, T., Sarantos, M., . . . Solomon, S. C. (2012, OCT 30). MESSENGER observations of a flux-transfer-event shower at Mercury [Article]. *J. Geophys. Res.*, *117*, A00M06. doi: {10.1029/2012JA017926}

Sun, W., Dewey, R. M., Aizawa, S., Huang, J., Slavin, J. A., Fu, S., . . . Bowers, C. F. (2022). Review of mercury's dynamic magnetosphere: Post-messenger era and comparative magnetospheres. *Science China Earth Sciences*, *65*(1), 25–74. Retrieved from https://doi.org/10.1007/s11430-021-9828-0 doi: 10.1007/s11430-021-9828-0

Sun, W., Slavin, J. A., Milillo, A., Dewey, R. M., Orsini, S., Jia, X., . . . Li, C. (2022). Messenger observations of planetary ion enhancements at mercury's northern magnetospheric cusp during flux transfer event showers. *Journal of Geophysical Research: Space Physics*, *127*(4), e2022JA030280. Retrieved from https://agupubs.onlinelibrary.wiley.com/doi/abs/10.1029/2022JA030280 (e2022JA030280 2022JA030280) doi: https://doi.org/10.1029/2022JA030280

Sun, W. J., Raines, J. M., Fu, S. Y., Slavin, J. A., Wei, Y., Poh, G. K., . . . Wan, W. X. (2017). Messenger observations of the energization and heating of protons in the near-mercury magnetotail. *Geophysical Research Letters*, *44*(16), 8149-8158. Retrieved from https://agupubs.onlinelibrary.wiley.com/doi/abs/10.1002/2017GL074276 doi: 10.1002/2017GL074276

Sun, W.-J., Slavin, J. A., Fu, S., Raines, J. M., Sundberg, T., Zong, Q.-G., . . . Zurbuchen, T. H. (2015). Messenger observations of alfvénic and compressional waves during mercury's substorms. *Geophysical Research Letters*, *42*(15), 6189-6198. Retrieved from https://agupubs.onlinelibrary.wiley.com/doi/abs/10.1002/2015GL065452 doi: https://doi.org/10.1002/2015GL065452

Sundberg, T., Boardsen, S. A., Slavin, J. A., Anderson, B. J., Korth, H., Zurbuchen, T. H., . . . Solomon, S. C. (2012). MESSENGER orbital observations of large-amplitude Kelvin-Helmholtz waves at Mercury's magnetopause. *J. Geophys. Res.*, *117*(A4), A04216. Retrieved from https://agupubs.onlinelibrary.wiley.com/doi/abs/10.1029/2011JA017268 doi: 10.1029/2011JA017268

Vasyliunas, V. (1968). A Survey of Low-Energy Electrons in the Evening Sector of the Magnetosphere with OGO 1 and OGO 3 [Article]. *J. Geophys. Res.*, *73*(9),

Figure 1. BepiColombo trajectory (a) projected on the X_{MSM}-Y_{MSM} plane, (b) mapped to the planet surface along magnetic field lines predicted from the KT17 model (Korth et al., 2017) as a function of the foot point MLT and the foot point geographic latitude, and projected on the (c) X_{MSM}-Z_{MSM} and (d) Y_{MSM}-Z_{MSM} planes. The curved line labeled "B-line magnetic equator mapping" in Figure 1a shows a magnetic field line mapping to the magnetic equator ($Z_{\mathrm{MSM}} = 0$). We use the instantaneous heliocentric distance and a disturbance index (DI) of 100 as input parameters for the KT17 model. In Figures 1a, 1c, and 1d, the colored, thin curves show the KT17 model field lines traced from the spacecraft position, and the black fans indicate the effective field of view of MIA during the observation. The gray curve in Figure 1a shows the KT17 model magnetopause. The dashed line in Figure 1b shows the open-closed boundary at which the traced field line distance exceeds $10R_M$ (Korth et al., 2014). The gray curves in Figure 1c show the KT17 model field lines on the X_{MSM}-Z_{MSM} plane.

2839-2884. doi: {10.1029/JA073i009p02839}

Winslow, R. M., Anderson, B. J., Johnson, C. L., Slavin, J. A., Korth, H., Purucker, M. E., ... Solomon, S. C. (2013). Mercury's magnetopause and bow shock from MESSENGER Magnetometer observations. *J. Geophys. Res.*, *118*(5), 2213-2227. Retrieved from `https://agupubs.onlinelibrary.wiley.com/doi/abs/10.1002/jgra.50237` doi: 10.1002/jgra.50237

Winslow, R. M., Johnson, C. L., Anderson, B. J., Gershman, D. J., Raines, J. M., Lillis, R. J., ... Zuber, M. T. (2014). Mercury's surface magnetic field determined from proton-reflection magnetometry. *Geophys. Res. Lett.*, *41*(13), 4463–4470. Retrieved from `http://dx.doi.org/10.1002/2014GL060258` doi: 10.1002/2014GL060258

Yokota, S., Saito, Y., Asamura, K., Tanaka, T., Nishino, M. N., Tsunakawa, H., ... Terasawa, T. (2009). First Direct Detection of Ions Originating from the Moon by MAP-PACE IMA Onboard SELENE (KAGUYA). *Geophys. Res. Lett.*, *36*, L11201. doi: 10.1029/2009GL038185

Zhang, C., Rong, Z. J., Gao, J. W., Zhong, J., Chai, L. H., Wei, Y., ... Wan, W. X. (2020). The flapping motion of mercury's magnetotail current sheet: Messenger observations. *Geophysical Research Letters*, *47*(4), e2019GL086011. Retrieved from `https://agupubs.onlinelibrary.wiley.com/doi/abs/10.1029/2019GL086011` (e2019GL086011 2019GL086011) doi: https://doi.org/10.1029/2019GL086011

Zhao, J.-T., Zong, Q.-G., Slavin, J. A., Sun, W.-J., Zhou, X.-Z., Yue, C., ... Ip, W.-H. (2020). Proton properties in mercury's magnetotail: A statistical study. *Geophysical Research Letters*, *47*(19), e2020GL088075. Retrieved from `https://agupubs.onlinelibrary.wiley.com/doi/abs/10.1029/2020GL088075` (e2020GL088075 10.1029/2020GL088075) doi: https://doi.org/10.1029/2020GL088075

Zhao, J. T., Zong, Q. G., Yue, C., Sun, W. J., Zhang, H., Zhou, X. Z., ... Wei, Y. (2022). Observational evidence of ring current in the magnetosphere of mercury. *Nature Communications*, *13*(1), 924. Retrieved from `https://doi.org/10.1038/s41467-022-28521-3` doi: 10.1038/s41467-022-28521-3

Figure 2. BepiColombo Mio observations of low-energy ions during the first Mercury flyby. (a) Energy-time spectrogram of ions in units of differential energy flux (eV/cm^2/s/sr/eV) obtained by MIA with its nominal 4 s resolution, (b) quasi-1 s resolution data that are available only during the cruise phase, KT17 model predictions (Korth et al., 2017) of (c) pitch angle coverage of the effective field of view of MIA (black) and critical pitch angles of parallel and anti-parallel loss cones (magenta), (d) three components and magnitude of the magnetospheric magnetic field, and (e) gyroradii of 1 keV H^+ (blue) and Na^+ (red) ions as well as the spacecraft altitudes (black). The text label indicates the magnetic local time (MLT) and magnetic latitude (MLat) of the spacecraft position in the aberrated Mercury Solar Magnetospheric (MSM) coordinates as defined in Anderson et al. (2013). The horizontal bars in Figures 2a and 2b indicate the time intervals analyzed in detail in Figure 3.

Figure 3. Detailed analyses of MIA data. Ion energy spectra obtained during (a) 23:13:26–23:13:42 UTC, (b) 23:16:20–23:16:36 UTC, (c) 23:30:00–23:30:16 UTC, and (d) 23:32:33–23:32:49 UTC. The colored lines show Maxwellian and kappa distribution fits to the data under the assumption of isotropy, proton-only composition, and a constant background (which is estimated from the average count rate at the two highest energy channels during 23:29–23:25 UTC). Two component distributions are assumed for Figures 3a (a cold Maxwellian and a hot kappa distribution) and 3c (two Maxwellian), while one component kappa distribution is used for Figures 3b and 3d. The best fit parameters are also shown (N is the density, T is the temperature, and kappa is the kappa parameter with subscripts c and h denoting the cold and hot components). MIA observations of rapid variations of ion fluxes (d) at 3130 eV/q during 23:29:50–23:30:20 UTC, (e) at 1795 eV/q during 23:31:50–23:32:20 UTC, and (f) at 210 eV/q during 23:40:30–23:41:10 UTC on 1 October 2021. The black lines show the quasi-1 s resolution data, while the blue lines show the nominal 4 s resolution data. The horizontal bars in Figures 3f and 3g denote the proton gyroperiod (T_{gp}) and the proton gyroradius divided by the spacecraft velocity (r_{gp}/V_{SC}) according to the magnetic field magnitude predicted from the KT17 model. In all panels, the error bars indicate uncertainties due to counting statistics.

Figure 1.

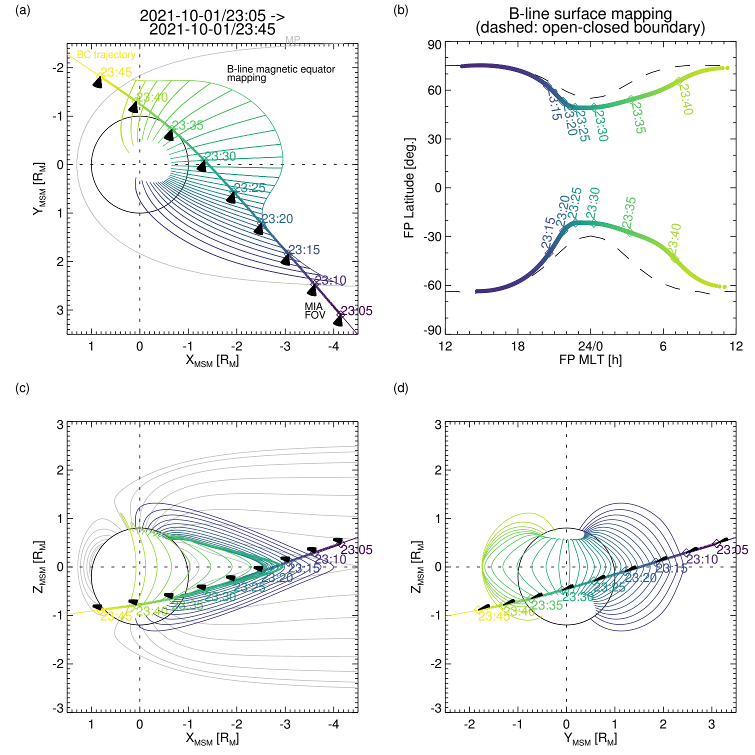
(a)
2021-10-01/23:05 ->
2021-10-01/23:45
MP
BC trajectory
B-line magnetic equator mapping
MIA FOV
23:05
23:10
23:15
23:20
23:25
23:30
23:35
23:40
23:45
X_{MSM} [R_M]
Y_{MSM} [R_M]
(b)
B-line surface mapping
(dashed: open-closed boundary)
FP Latitude [deg.]
FP MLT [h]
12
18
24/0
6
12
(c)
X_{MSM} [R_M]
Z_{MSM} [R_M]
(d)
Y_{MSM} [R_M]
Z_{MSM} [R_M]

Figure 2.

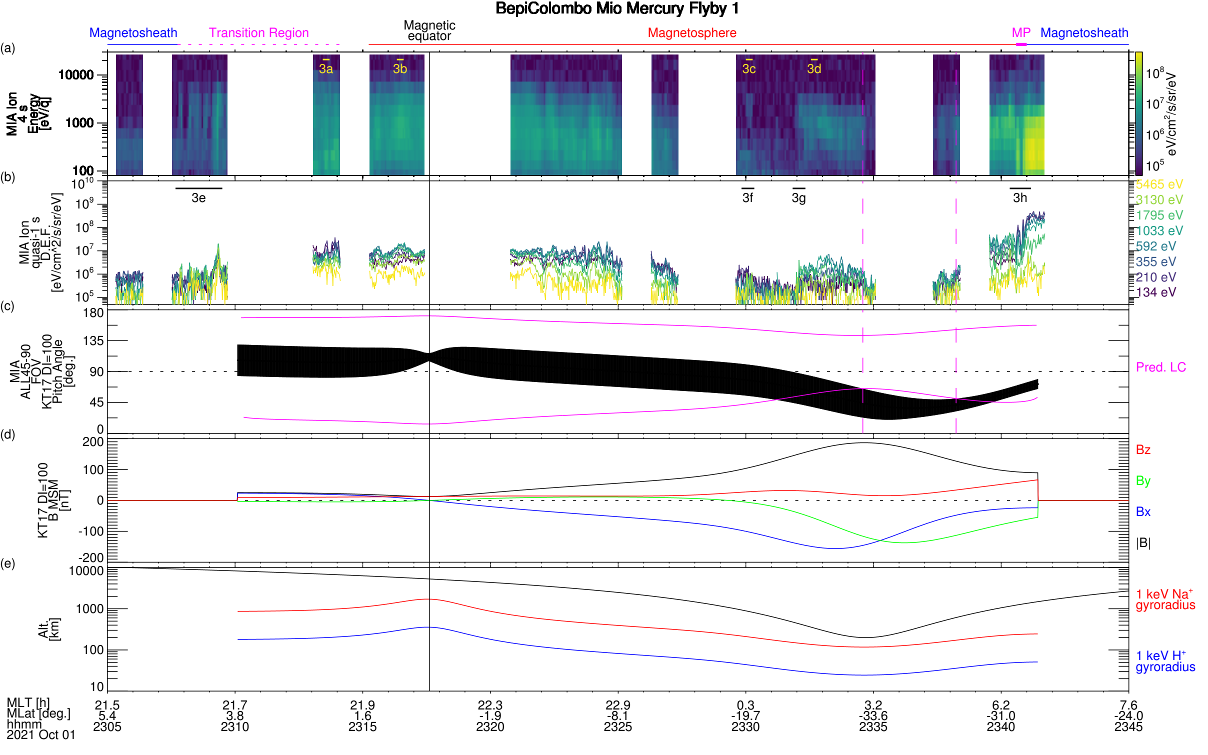
BepiColombo Mio Mercury Flyby 1
Magnetosheath
Transition Region
Magnetic equator
Magnetosphere
MP
Magnetosheath
(a)
MIA Ion 4 s Energy [eV/q]
3a
3b
3c
3d
eV/cm^2/s/sr/eV
(b)
MIA Ion quasi-1 s D.E.F. [eV/cm^2/s/sr/eV]
3e
3f
3g
3h
5465 eV
3130 eV
1795 eV
1033 eV
592 eV
355 eV
210 eV
134 eV
(c)
MIA ALL45-90 FOV KT17 DI=100 Pitch Angle [deg.]
Pred. LC
(d)
KT17 DI=100 B MSM [nT]
Bz
By
Bx
|B|
(e)
Alt. [km]
1 keV Na+ gyroradius
1 keV H+ gyroradius
MLT [h]
MLat [deg.]
hhmm
2021 Oct 01

Figure 3.

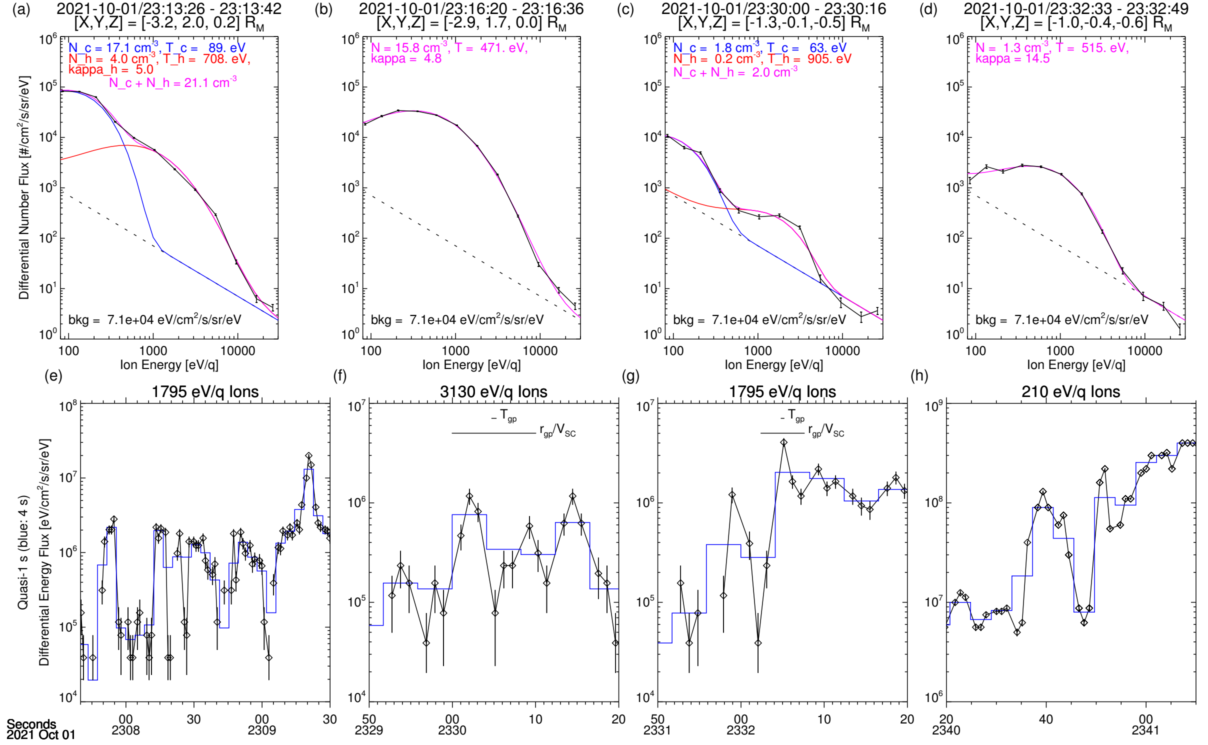

(a)
2021-10-01/23:13:26 - 23:13:42
[X,Y,Z] = [-3.2, 2.0, 0.2] R_M
N_c = 17.1 cm^-3, T_c = 89. eV
N_h = 4.0 cm^-3, T_h = 708. eV,
kappa_h = 5.0
N_c + N_h = 21.1 cm^-3
bkg = 7.1e+04 eV/cm^2/s/sr/eV
(b)
2021-10-01/23:16:20 - 23:16:36
[X,Y,Z] = [-2.9, 1.7, 0.0] R_M
N = 15.8 cm^-3, T = 471. eV,
kappa = 4.8
bkg = 7.1e+04 eV/cm^2/s/sr/eV
(c)
2021-10-01/23:30:00 - 23:30:16
[X,Y,Z] = [-1.3,-0.1,-0.5] R_M
N_c = 1.8 cm^-3, T_c = 63. eV
N_h = 0.2 cm^-3, T_h = 905. eV
N_c + N_h = 2.0 cm^-3
bkg = 7.1e+04 eV/cm^2/s/sr/eV
(d)
2021-10-01/23:32:33 - 23:32:49
[X,Y,Z] = [-1.0,-0.4,-0.6] R_M
N = 1.3 cm^-3, T = 515. eV,
kappa = 14.5
bkg = 7.1e+04 eV/cm^2/s/sr/eV
Differential Number Flux [#/cm^2/s/sr/eV]
Ion Energy [eV/q]
(e)
1795 eV/q Ions
(f)
3130 eV/q Ions
T_gp
r_gp/V_SC
(g)
1795 eV/q Ions
T_gp
r_gp/V_SC
(h)
210 eV/q Ions
Quasi-1 s (blue: 4 s)
Differential Energy Flux [eV/cm^2/s/sr/eV]
Seconds
2021 Oct 01